ACS OMEGA

http://pubs.acs.org/journal/acsodf

Article

Cu Species-Modified OMS-2 Materials for Enhancing Ozone Catalytic Decomposition under Humid Conditions

Chonglai Chen, Jun Xie, Xiao Chen,* Wenxia Zhang, Jian Chen, and Aiping Jia*

Cite This: *ACS Omega* 2023, 8, 19632−19644

Read Online

ACCESS | Metrics & More | Article Recommendations

ABSTRACT: Manganese oxide octahedral molecular sieves (OMS-2) exhibit an excellent performance in ozone catalytic decomposition in dry atmosphere conditions, which however is severely limited by deactivation in humid conditions. Herein, it was found that the OMS-2 materials modified with Cu species could obviously improve both the ozone decomposition activity and water resistance. Based on the characterization results, it was found that these CuO_x/OMS-2 catalysts exhibited dispersed CuO_x nanosheets attached and located at the external surface accompanied with ionic Cu species entering the MnO_6 octahedral framework of OMS-2. In addition, it was demonstrated that the main reason for the promotion of ozone catalytic decomposition could be ascribed to the combined effect of different Cu species in these catalysts. On the one hand, ionic Cu entered the MnO_6 octahedral framework of OMS-2 near the catalyst surface and substituted ionic Mn species, resulting in an enhanced mobility of surface oxygen species and formation of more oxygen vacancies, which act as the active sites for ozone decomposition. On the other hand, the CuO_x nanosheets could serve as non-oxygen vacancy sites for H_2O adsorption, which could alleviate the catalyst deactivation to some extent caused by the occupancy of H_2O on surface oxygen vacancies. Finally, different reaction pathways for ozone catalytic decomposition over OMS-2 and CuO_x/OMS-2 under humid conditions were proposed. The findings in this work may shed new light on the design of highly efficient catalysts for ozone decomposition with improved water resistance.

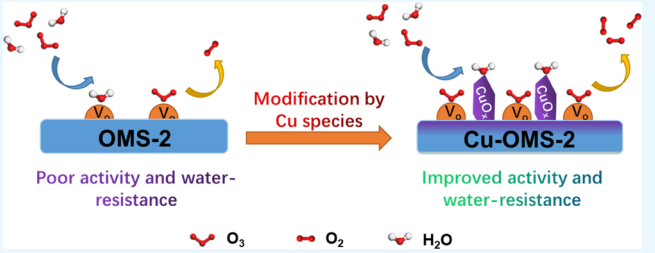

1. INTRODUCTION

As we all know, stratospheric ozone (O_3) can prevent strong ultraviolet radiation from reaching the earth. However, ozone near the ground becomes a kind of pollution gas, which can not only cause damage to the ecosystem[1,2] but also have certain destructive effects on human health.[3−5] Therefore, it is very necessary to decompose it into harmless substances thus to meet the emission standard of 0.08 ppm as the Chinese indoor air quality standard (GB/T18883-2002) specifies[6] or the average allowable contact gaseous ozone concentration of only 100 $\mu g\ m^{-3}$ (~51 ppb) in 8 h as the World Health Organization (WHO) has established,[7] which is of practical significance to eco-environmental protection and public health.

In the past decades, a large number of techniques and methods have been developed for the decomposition of ozone from the air.[8,9] Among these, catalytic decomposition is considered as the most effective way to eliminate ozone due to its high efficiency, safety, and low cost.[10−12] Generally speaking, there are two different types of active components in catalysts, which are applied to the ozone catalytic decomposition, i.e., noble metals such as Pd,[13] Au,[14] and Ag[15] and nonprecious metal oxides such as Fe,[16] Co,[17,18] Ni,[19] and Mn.[20] Among these, the manganese oxide octahedral molecular sieves (OMS-2), which possess a 2 × 2 tunnel structure (4.6 Å × 4.6 Å) consisting of MnO_6 octahedral chains, have attracted much interest in ozone catalytic decomposition due to their large specific surface area, low cost, environmental friendliness, and superior catalytic activity.[21] Nevertheless, the catalytic performance of OMS-2 could be significantly inhibited by water vapor at high GHSV, which limits their practical application.[21,22] Modification of the OMS-2 material with other metal ions such as transition metals,[23−25] noble metals,[6] and alkali metals[26] is the common way to promote the catalytic performance as the concentration of surface oxygen vacancies can be obviously raised, which have been extensively deemed as the active center for ozone catalytic decomposition.[27−29] For example, Ma et al.[25] investigated a series of OMS-2 materials doped with transition metals such as cerium, cobalt, and iron and found that cerium-doped OMS-2 materials gave the best performance and the Mn^{3+} content and the amount of surface defects played a key role in the ozone catalytic decomposition. Nevertheless, the

Received: February 21, 2023
Accepted: May 10, 2023
Published: May 22, 2023

activity of Ce-OMS-2 was not satisfactory at high GHSV and high humidity.[23,24] Yang et al.[6] continued to dope Ce-OMS-2 with Pd, which improved the ozone removal performance of the catalysts in a humid environment due to the increase in oxygen vacancy concentration caused by Pd−Mn interactions. However, the use of noble metals as dopants will reduce the economic efficiency of catalysts. Therefore, it is an urgent need to develop nonprecious metal doping catalysts under humid conditions. Moreover, to the best of our knowledge, the study of OMS-2 materials modified with a common nonprecious metal such as copper have not yet been reported in the ozone catalytic decomposition, especially under humid conditions.

In recent years, copper-doped OMS-2 materials have been frequently reported in many industrial areas due to their excellent performance. For example, Li et al.[30] found that the catalytic active phases of the CuO/OMS-2 nanocomposite were reconstructed to metallic Cu and Mn_3O_4 when the reaction temperature exceeded 240 °C, which exhibited highly efficient catalytic activity for NO reduction by CO to N_2. Liu et al.[31] found that the optimal CuO/OMS-2 catalyst provides reactivity with a T_{90} of 55 °C and the interaction between the highly dispersed CuO and OMS-2 support generates active sites for CO oxidation. Yu et al.[32] also reported a practical protocol for efficiently preparing diaryl sulfides using Cu-OMS-2 to catalyze the C−S coupling reactions of substituted thiophenols and aryl halides. Recently, Han et al.[33] reported that both the catalytic performance for mercury removal and the sulfur resistance ability could be improved by modification of OMS-2 using copper. Our preliminary experiment had discovered that the modification of OMS-2 with copper could significantly improve the ozone decomposition activity of the catalyst under humid conditions. However, the relationship between the catalyst structure and the performance for ozone catalytic decomposition has not been established yet.

Specifically, two different synthetic strategies could be employed to modify the OMS-2 with the copper species, i.e., the preincorporation and wet impregnation methods. The former as commonly employed in extensive studies will control the localization of Cu species in the interior of OMS-2 (i.e., Cu-OMS-2), while the latter performs on the external surface (i.e., CuO_x/OMS-2). In this work, the wet impregnation method was preferred to be employed to prepare a series of CuO_x/OMS-2 catalysts with different contents of Cu species to modify the external surface properties of OMS-2 and the enhancement effect of Cu species on ozone catalytic decomposition under humid conditions was investigated. The position of Cu species in OMS-2 was determined using a variety of characterization techniques, and the key factors influencing the catalytic performance were unveiled. Based on these findings, different reaction pathways for ozone catalytic decomposition over unsupported OMS-2 and CuO_x/OMS-2 under a humid atmosphere were proposed. Although the catalysts reported in this work were not superior to the best catalysts reported to date, this work would provide a reference for the design of highly efficient catalysts to eliminate ozone under humid conditions.

2. EXPERIMENTAL SECTION

2.1. Chemicals and Reagents. $KMnO_4$, $MnSO_4{\cdot}H_2O$, and $Cu(NO_3)_2{\cdot}3H_2O$ were purchased from the Sinopharm Chemical Reagent Co. Ltd., China. All these reagents were analytical grade and used without further purification.

2.2. Catalyst Preparation. In this work, a series of CuO_x/OMS-2 catalysts modified with different contents of Cu species were prepared by a simple impregnation method. First, the OMS-2 powder was synthesized by a facile redox reaction between the $KMnO_4$ as an oxidant and the $MnSO_4$ as a reductant. In a typical synthesis, $MnSO_4{\cdot}H_2O$ (8.8 g) was dissolved in deionized water (30 mL) in a beaker; then, concentrated nitric acid (3 mL) was added to the above-mentioned solution under stirring. $KMnO_4$ (5.89 g) was dissolved in deionized water (100 mL) and slowly added to the above-mentioned mixed solution and then was continuously stirred with a magnetic agitator for 0.5 h and then left to rest for 0.5 h to precipitate the black-brown solids. Then, the obtained solids were rinsed with deionized water repeatedly until there was no residual SO_4^{2-} in the filtrate (detected using 0.2 mol L^{-1} $BaCl_2$ solution). After that, the obtained products were dried overnight at 110 °C to produce OMS-2 powder and divided into several groups. One group was calcined at 400 °C in static air for 4 h to produce the calcined OMS-2 material, and the others were employed as supports to prepare a series of CuO_x/OMS-2 catalysts with different contents of Cu species. For example, 1 g of OMS-2 was dispersed in a 5 mL $Cu(NO_3)_2$ solution with a certain concentration, and the mixture was stirred for 5 h at room temperature and evaporated to dryness using a water bath at 90 °C. Finally, the obtained solid was also dried at 110 °C and calcined at 400 °C in static air for 4 h, which was denoted as yCuO$_x$/OMS-2, where y represents the Cu/Mn molar ratio. Since the molar ratio of Cu/Mn in these catalysts was 0.01, 0.02, 0.05, and 0.1, these catalysts were designated as 0.01CuO$_x$/OMS-2, 0.02CuO$_x$/OMS-2, 0.05CuO$_x$/OMS-2, and 0.1CuO$_x$/OMS-2, respectively. For comparison, some CuO_x powders were also prepared by direct evaporation of $Cu(NO_3)_2$ solution using a water bath and dried and calcined in the same way.

2.3. Characterization of Catalysts. The actual Cu contents in the catalysts were determined using an Optima 7300DV inductively coupled plasma atomic emission spectrometer (ICP-AES). The phase structures of the catalyst samples were characterized using a Bruker D8 ADVANCE X-ray powder diffractometer (XRD) by using Cu Kα radiation (λ = 1.5418 Å) working at 40 kV and 40 mA. The patterns were collected in the scanning range from 10 to 90° with a scanning rate of 0.05° s^{-1}. The Raman spectra of the samples were recorded on a Renishaw inVia-Reflex instrument by employing a 532 nm laser source at a power of 3 mW. The dwell time was 90 s, the number of scans was 1, and the resolution was 1 cm^{-1}. Field emission scanning electron microscopy (FESEM) coupled with energy dispersive X-ray spectroscopy (EDX) was performed to investigate the microstructure and compositional distribution of the catalysts using a ZEISS Gemini SEM 300 scanning electron microscope, which was operated at an accelerating voltage of 5 and 15 kV. Transmission electron microscopy (TEM) and high-resolution transmission electron microscopy (HRTEM) were conducted on a JEOL JEM-2100F instrument operated at 200 kV. The N_2 adsorption−desorption experiments at 77 K were carried out on a Quantachrome Nova 4000e surface area analyzer. The specific surface area was determined by the Brunauer−Emmett−Teller (BET) method, and the pore size distribution was calculated by using the Barrett−Joyner−Halenda (BJH) formula from the desorption branch of the isotherms. Before the test, all the samples were degassed at 200 °C. The surface properties of these catalysts were analyzed using a ThermoFisher ESCALAB

https://doi.org/10.1021/acsomega.3c01186
ACS Omega 2023, 8, 19632−19644

Scheme 1. Schematic Diagram of the Experimental Setup for the Ozone Catalytic Decomposition Measurement

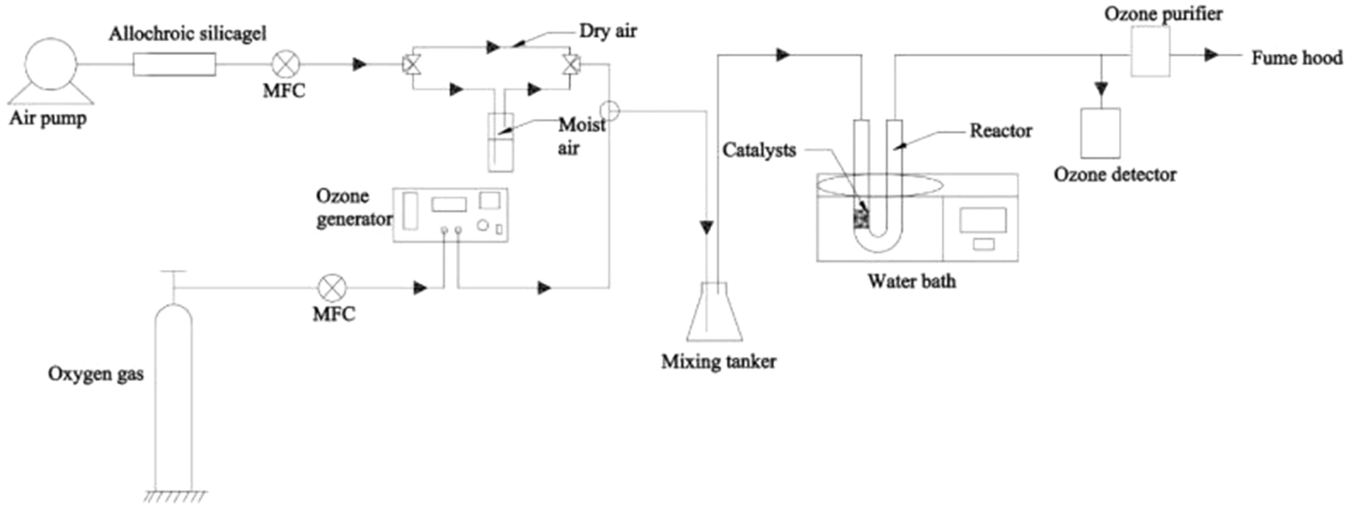

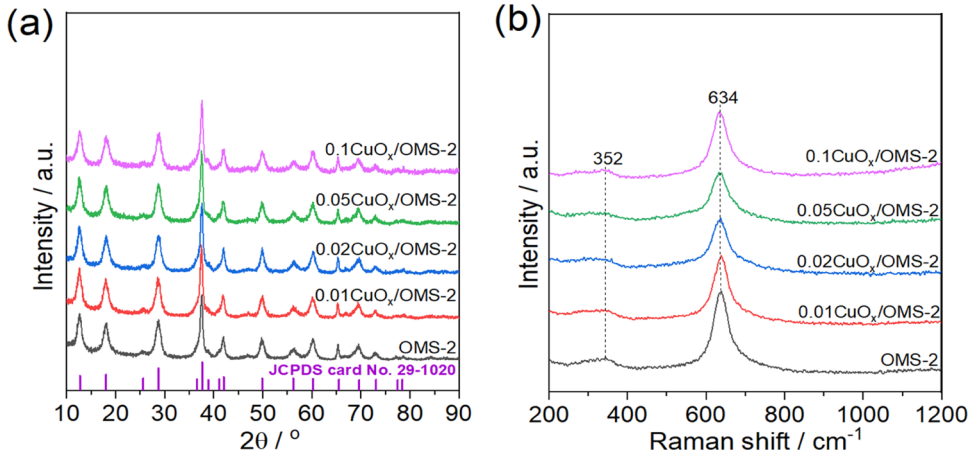

Figure 1. XRD patterns (a) and Raman spectra (b) of various samples.

250Xi X-ray photoelectron spectrometer (XPS) with a monochromatic Al anode Kα radiation (hυ = 1486.6 eV) as the excitation light source and calibrated internally by setting the C1s binding energy of the adventitious carbon to 284.8 eV. The water contact angle measurement was carried out on a Sindin SDC-100-type contact angle-measuring device.

The reducibility of the catalyst was measured using a homemade hydrogen temperature-programmed reduction (H_2-TPR) experiment. In the typical H_2-TPR experiment, 50 mg of the catalyst was loaded in a quartz tubular reactor and was heated to 300 °C in a pure N_2 (99.99%, 30 mL min^{-1}) flow and kept in a flow of pure N_2 (99.99%) for 0.5 h to clean the catalyst surface. After the sample was cooled to room temperature, it was heated to 800 °C at a rate of 10 °C min^{-1} in a 5% H_2−95% N_2 mixture (30 mL min^{-1}). The signal was recorded using a thermal conductivity detector (TCD), and the H_2 consumption was calibrated by the reduction of CuO powder with a known amount.

O_2 temperature-programmed desorption (O_2-TPD) experiments were conducted on a MicrotracBEL Belcat II automatic chemisorption analyzer. In the typical O_2-TPD experiment, 50 mg of the sample was initially pretreated at 300 °C under a He flow (30 mL min^{-1}) for 0.5 h to remove the surface-adsorbed H_2O. After cooling to room temperature (25 °C), the sample was further purged with a 5 vol % O_2/He mixture (30 mL min^{-1}) for 1 h, followed by switching automatically to the He flow for purging for 1 h to remove the residual gaseous and/or physically adsorbed O_2. Thereafter, the desorption of O_2 in the sample was carried out from 30 to 700 °C with a heating rate of 10 °C min^{-1}, and the desorbed oxygen signal was collected.

Water temperature-programmed desorption (H_2O-TPD) experiments were performed in a quartz tube reactor system equipped with a Hiden QIC-20 MS. In the typical H_2O-TPD experiment, 200 mg of the sample was also initially pretreated at 300 °C under a He flow (30 mL min^{-1}) for 0.5 h to remove the surface-adsorbed H_2O and then cooled to room temperature; then, the H_2O-TPD experiment was performed by passing He through a saturator containing pure water for 1 h at 25 °C. After water adsorption, the sample was purged using He for at least 1 h to remove the physically adsorbed water. The desorption of the chemically adsorbed water was conducted by heating the sample to 550 °C at a rate of 10 °C min^{-1}, and the detection of the desorbed water (m/e = 18) was monitored using a mass spectrometer.

2.4. Ozone Decomposition Measurement. The ozone catalytic decomposition experiments were performed on a laboratory-made setup with a fixed-bed quartz U-tube reactor (i.d. 8 mm) using 0.1 g of catalyst at room temperature (25 °C), as illustrated in Scheme 1. The total flow velocity of the feed gas was controlled at 1000 mL min^{-1}, thus giving the

https://doi.org/10.1021/acsomega.3c01186
ACS Omega 2023, 8, 19632−19644

weight hourly space velocity (WHSV) of 600 000 mL g^{-1} h^{-1}. A bubbler was kept at a certain temperature to maintain a certain relative humidity (RH). The temperature of the reactor was maintained using a thermos static water bath. Ozone in the inlet gas was generated using ultraviolet lamps (COM-AD-01-OEM, Anseros, Germany), and the inlet ozone concentration was 50 ± 2 ppm. The ozone concentration in inlet and outlet gases was detected using an ozone gas analyzer (BMOT-200T, Weifang Shengxin Electronics, China) with a detection limit of 0.1 ppm. The ozone conversion was calculated according to the following equation

$$\text{ozone conversion}\ (\%) = (C_{\text{inlet}} - C_{\text{outlet}})/C_{\text{inlet}} \times 100\% \quad (1)$$

where C_{inlet} and C_{outlet} are the concentrations of ozone detected at the inlet and outlet, respectively.

3. RESULTS AND DISCUSSION

3.1. Crystal Structure, Morphology, and Textural Properties. XRD patterns of the unsupported OMS-2 materials and yCuO$_x$/OMS-2 catalysts are shown in Figure 1a. All these samples showed the characteristic diffraction of peaks at 12.7, 18.1, 28.7, 37.6, 42.0, and 49.9°, which corresponded to the cryptomelane-type manganese dioxide (JCPDS 29-1020).[34] No extra peaks attributed to CuO$_x$ (x = 0.5 or 1) species were observed even over the 0.1CuO$_x$/OMS-2 catalysts with the highest Cu content as shown in Table 1,

Table 1. Actual Cu Content and N_2 Adsorption−Desorption Results of Various Samples

samples	Cu content[a] (wt %)	BET surface area (m^2 g^{-1})	total pore volume (cm^3 g^{-1})	average pore diameter (nm)
OMS-2		134.7	0.224	6.6
0.01CuO$_x$/OMS-2	0.79	127.5	0.345	9.4
0.02CuO$_x$/OMS-2	1.65	126.0	0.339	10.1
0.05CuO$_x$/OMS-2	3.90	123.6	0.325	10.5
0.1CuO$_x$/OMS-2	7.92	102.5	0.305	11.9

[a]The Cu content in catalysts was determined by ICP.

indicating that these Cu species were highly dispersed on the catalyst surface or incorporated into the structure. However, no obvious difference in the peak intensity or shift between these catalysts could be discovered, suggesting that the modification of Cu species had little effect on the bulk phase of OMS-2 and the unique cryptomelane structure can be maintained over these CuO$_x$/OMS-2 catalysts. The grain size of the unsupported OMS-2 materials and yCuO$_x$/OMS-2 catalysts can be calculated through the Scherrer formula ($D = 0.89\lambda/(B\cos\theta)$), where their grain size was all around 14.0 nm. Nevertheless, the possibility of ionic Cu species entering the MnO$_6$ octahedral framework near the catalyst surface could not be excluded as the radii of Cu^+ (0.77 Å)[35] and Cu^{2+}(0.73 Å)[36] are nearly the same as those of Mn^{3+} (0.72 Å) and Mn^{4+} (0.67 Å).[37] In other words, it is theoretically feasible for Cu ions substituting Mn ions in the octahedral framework near the catalyst surface.

Compared with XRD, Raman spectroscopy is a technique that is more sensitive to the surface property of samples. Figure 1b shows the Raman spectra of the unsupported OMS-2 materials and yCuO$_x$/OMS-2 catalysts, which gave similar bands at 352 and 634 cm^{-1}. The weak intensity of peaks at 352 cm^{-1} corresponded to the deformation modes of the metal−oxygen chain of Mn−O−Mn, while the distinct bands at 634 cm^{-1} originated from the symmetrical stretching vibration of Mn−O in the MnO$_6$ octahedra.[38−41] Furthermore, no signals due to the crystal or polycrystal of Cu species could be observed, consistent with the XRD results. However, the Raman spectra of these yCuO$_x$/OMS-2 catalysts were broadened and decreased gradually in intensity as the Cu/Mn molar ratio increased from 0.01 to 0.05 in comparison to those of the unsupported OMS-2 material, suggesting that ionic Cu species entered the MnO$_6$ octahedra framework of OMS-2 and notably weakened the stretching mode of the Mn−O lattice. Earlier studies had found that Cu in the Cu-OMS-2 structure can provoke the weakening of the Mn−O bond by electronic delocalization on the Cu−O−Mn bridges, which was favorable for the promotion of high oxygen lability and the formation of oxygen defects.[42,43] However, further increasing the Cu/Mn molar ratio to 0.1 was not conducive for Cu species to enter the MnO$_6$ octahedral framework of OMS-2 over the 0.1CuO$_x$/OMS-2 catalyst, which gave sharper and stronger intensity of Raman peaks compared to those of the 0.05CuO$_x$/OMS-2 catalyst. Nevertheless, these results demonstrated that partly, Cu species such as ionic Cu entered the framework of OMS-2 near the yCuO$_x$/OMS-2 catalyst surface and substituted ionic Mn species to form Cu-OMS-2, thus introducing more surface defects, which could favor ozone decomposition.

SEM images of the unsupported OMS-2 material and yCuO$_x$/OMS-2 catalysts are shown in Figure 2. Generally speaking, OMS-2 usually presents nanorod morphology in many studies[33,34,44,45] but also shows other morphologies, such as hydrangea,[13] nanoparticle,[46] and microsphere,[47] which may depend on their different synthesis details. The morphology of OMS-2 in this work as displayed by Figure 2a1,a2 presents the microsphere morphology with 200−300 nm diameter. However, the SEM images of CuO$_x$/OMS-2 catalysts showed a similar microsphere morphology as shown in Figure 2b1−d1 with some dispersed CuO$_x$ nanosheets with ca. 100 nm diameter attached and located on the external surface of OMS-2 as shown in Figure 2b2−d2. Meanwhile, the presence of Cu and O in these CuO$_x$ nanosheets was further confirmed by the inserted EDX mapping spectrum as shown in Figure 2d2. Furthermore, the increase of Cu/Mn molar ratios from 0.01 to 0.1 could promote the formation of growing number of CuO$_x$ nanosheets on the surface of OMS-2. In order to further verify the localization of Cu species in these yCuO$_x$/OMS-2 catalysts, the EDX mapping test of the 0.05CuO$_x$/OMS-2 catalyst as a representative has been carried out. As shown in Figure 2f1−f5, the EDX mapping of the Cu species distinctly exhibits the almost full morphology of the catalyst, suggesting that these Cu species were uniformly distributed on the surface of OMS-2.

To determine the exposed crystal facet of the CuO$_x$ nanosheets on these catalysts, we performed TEM and HRTEM tests of the 0.05CuO$_x$/OMS-2 catalyst as a representative sample, as shown in Figure 3. In Figure 3a, we observed nanosheet-type structures located on the surface of the catalyst, with average widths and lengths of 50 and 100 nm, respectively, consistent with the FESEM results. Moreover, the HRTEM image in Figure 3b revealed an interplanar spacing of 0.233 nm corresponding to the (111) planes of monoclinic CuO.[48]

https://doi.org/10.1021/acsomega.3c01186
ACS Omega 2023, 8, 19632−19644

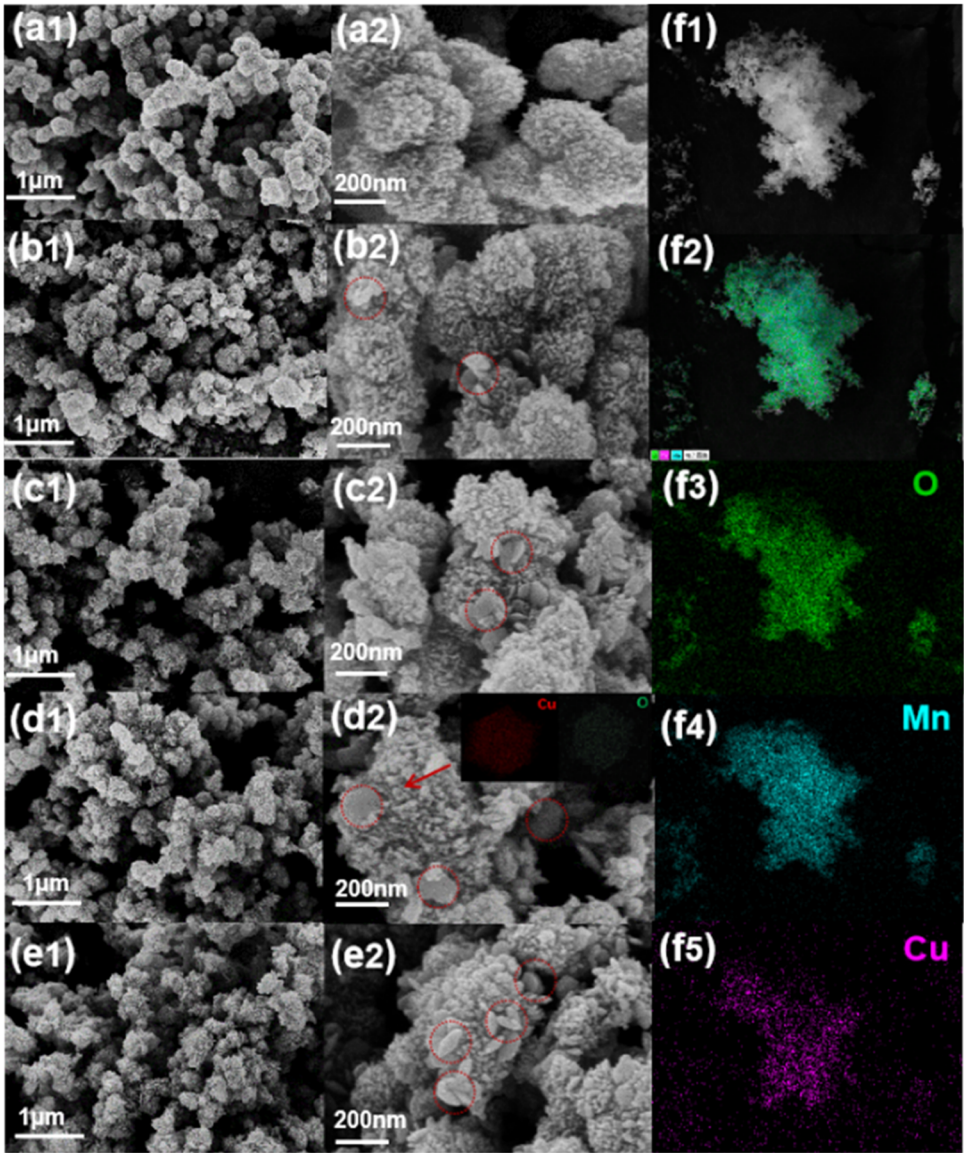

Figure 2. SEM images for unsupported OMS-2 (a1, a2), 0.01CuO_x/OMS-2 (b1, b2), 0.02CuO_x/OMS-2 (c1, c2), 0.05CuO_x/OMS-2 (d1, d2), and 0.1CuO_x/OMS-2 (e1, e2) and EDX mapping of 0.05CuO_x/OMS-2 (f1−f5).

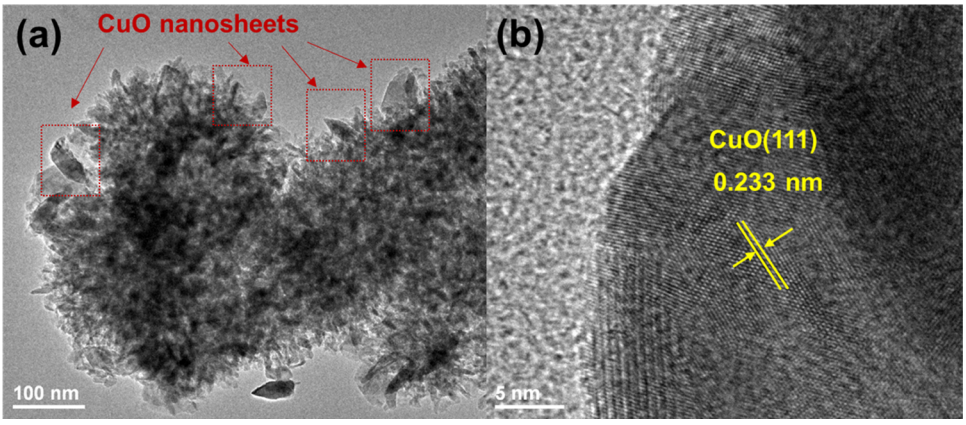

Figure 3. TEM images (a) and HRTEM image (b) of the 0.05CuO_x/OMS-2 catalyst.

The N_2 adsorption−desorption isotherms and pore size distributions of the unsupported OMS-2 material and yCuO_x/OMS-2 catalysts are analyzed in Figure 4a,b, respectively. The N_2 adsorption−desorption isotherms showed a characteristic type II isotherm pattern with a hysteresis loop of type H_3 based on the IUPAC classification, indicating the adsorption on

https://doi.org/10.1021/acsomega.3c01186
ACS Omega 2023, 8, 19632−19644

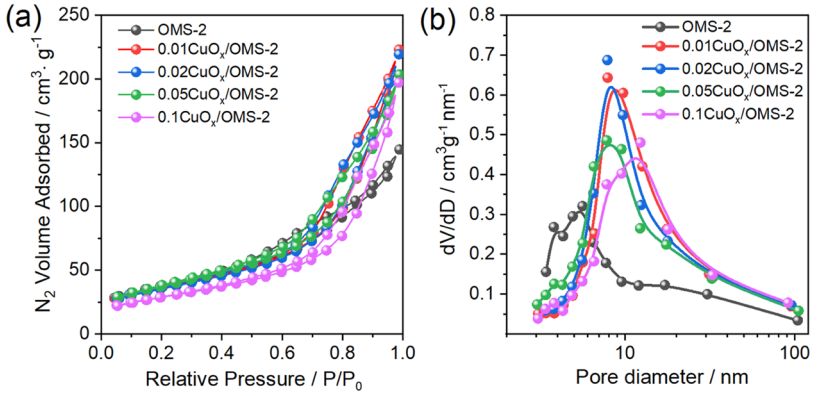

Figure 4. N_2 adsorption−desorption isotherms (a) and the pore size distribution (b) of various samples.

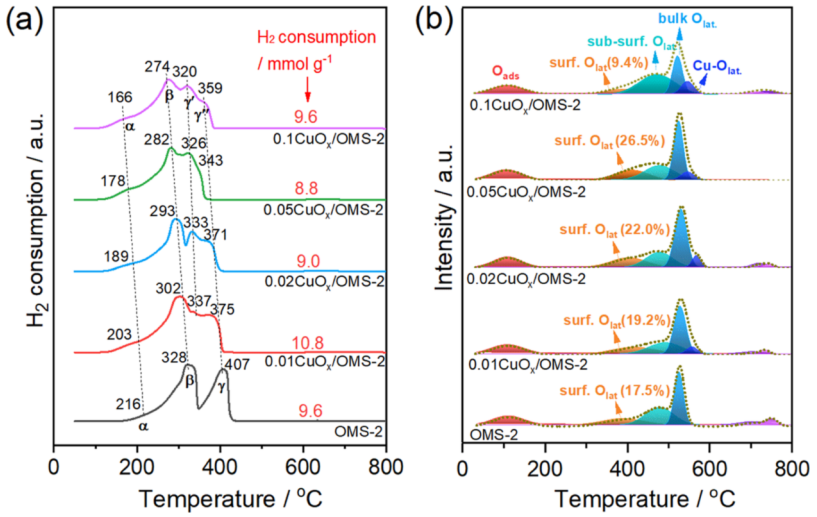

Figure 5. H_2-TPR (a) and O_2-TPD curves (b) of various samples.

aggregates of particles forming slit-like pores, similar to those previously reported for OMS-2.[25,49] The corresponding values of BET surface area, total pore volume, and average pore diameter are given in Table 1. It can be found that compared to that of unsupported OMS-2 (134.7 m^2 g^{-1}), the BET surface areas of $yCuO_x$/OMS-2 slightly decreased to 123.6−127.5 m^2 g^{-1} with lower Cu/Mn ratios (0.01−0.05) and then obviously to 102.5 m^2 g^{-1} with the highest Cu/Mn ratio (0.1), accompanied with the increase of their average pore diameter from 6.6 to 11.9 nm. These results demonstrate that these CuO_x species are mainly located on the external surface of OMS-2 with lower Cu/Mn ratios, gradually entering the channel pore structure of OMS-2 with the increase of Cu/Mn ratios, which thus block the channels of OMS-2, especially with the smaller pore size ones. This may be the main cause accounted for the worst activity of $0.1CuO_x$/OMS-2 catalysts compared to the counterparts as this excess amount of CuO_x species will cover the surface and/or block the channel pore structure of the catalysts, thus causing the decrease in the probability of ozone adsorption on the surface oxygen vacancy.

3.2. Temperature-Programmed Studies. Since the ozone catalytic decomposition ability of the catalysts is highly dependent on the reducibility of the catalysts, the reducibility of the OMS-2 sample and $yCuO_x$/OMS-2 catalysts was further determined by the H_2-TPR measurement as shown in Figure 5a. For the unsupported OMS-2, a weak peak at 216 °C (α) with two strong peaks at 328 °C (β) and 407 °C (γ) was observed. Among these, the α peak was ascribed to the reduction of surface oxygen species, which thus led to the partial reduction of MnO_2, while β and γ peaks were ascribed to the reduction of $MnO_2 \rightarrow Mn_3O_4 \rightarrow MnO$.[6,50] In the case of $yCuO_x$/OMS-2 catalysts, these three reduction peaks evolved into four peaks, i.e., α, β, and divided γ' and γ'', which were generally shifted to lower temperatures gradually with the increase of the Cu/Mn molar ratios. However, an exception could be observed that the position of the γ'' peak (359 °C) over the $0.1CuO_x$/OMS-2 sample is higher than that (343 °C) over $0.05CuO_x$/OMS-2, probably due to the obviously lower surface area of the former than that of the latter, which is thus not favorable for H_2 to complete the reduction of MnO_2 to MnO. These results indicated that the addition of Cu species promoted the reduction of MnO_2 and the interaction between Cu and Mn species was growing. However, the reduction peaks of a small amount of Cu species could be overlapped by the stepwise reduction process of OMS-2, which made it hard to distinguish. Due to the clearer α peaks appearing at low temperatures in these catalysts compared to those of unsupported OMS-2 materials, these α peaks were ascribed to the reduction of well-dispersed surface CuO_x species and the partial reduction of MnO_2 species, as the reducibility of CuO_x/OMS-2 could be improved by the spillover hydrogen from copper atoms to manganese oxides.[51] Moreover, the divided γ' and γ'' peaks further indicated that the Cu^{2+}−O−Mn^{4+} entities were generated at the interface

https://doi.org/10.1021/acsomega.3c01186
ACS Omega 2023, 8, 19632−19644

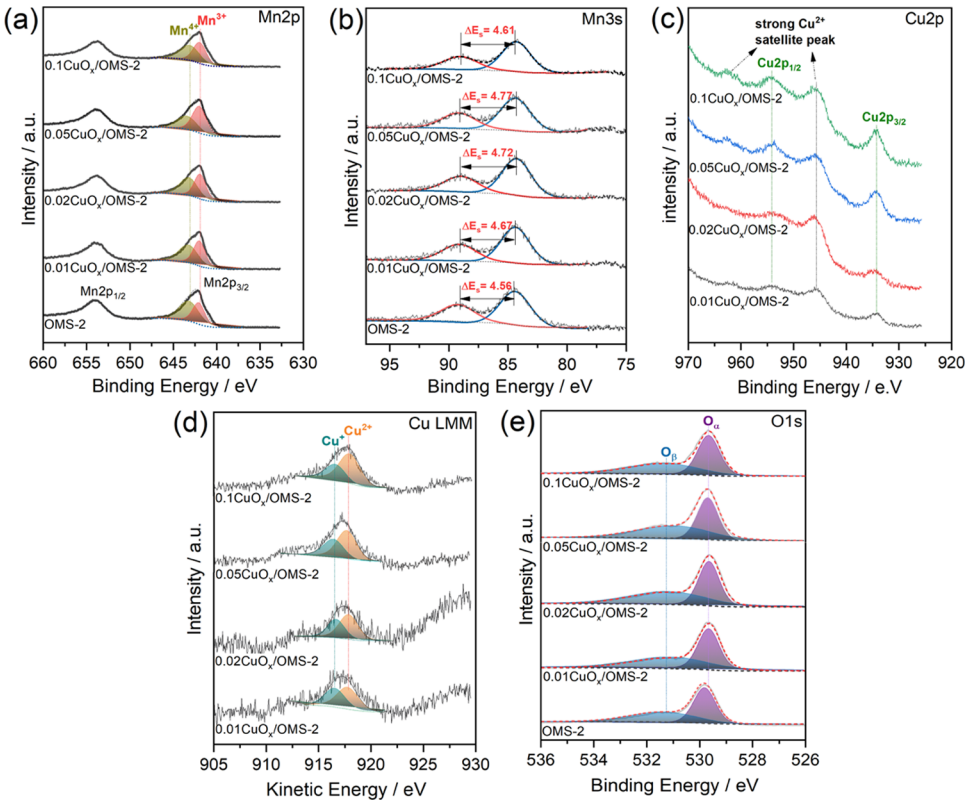

Figure 6. XPS spectra of Mn 2p (a), Mn 3s (b), Cu 2p (c), Cu LMM (d), and O 1s (e) of various samples.

Table 2. Each Component Ratio Based on the XPS Results of Various Samples

	Mn $2p_{3/2}$		Mn 3s	Cu LMM		O 1s[aa]		
samples	Mn^{3+} (%)	Mn^{4+} (%)	AOS	Cu^{1+} (%)	Cu^{2+} (%)	O_α (%)	O_β (%)	K/Mn molar ratio
OMS-2	40.5	59.5	3.82			53.4	46.6	0.04
0.01CuO_x/OMS-2	47.3	52.7	3.70	45.2	54.8	51.6	48.3	0.03
0.02CuO_x/OMS-2	50.2	49.2	3.64	40.4	59.6	49.4	50.6	0.03
0.05CuO_x/OMS-2	58.8	41.2	3.58	38.9	61.1	48.5	51.5	0.03
0.1CuO_x/OMS-2	46.9	53.1	3.77	32.0	68.0	54.3	45.7	0.03

[a]O_α, lattice oxygen (O^{2-}); O_β: surface oxygen (O^-, O^{2-}) adsorbed on oxygen vacancies.

between CuO_x and OMS-2, which gave a better reducibility compared to that of OMS-2.[50−52] Besides, the amounts of H_2 consumption by different samples are also listed in Figure 4a, which were obviously smaller than the theoretical value (11.5 mmol·g^{-1}) for the reduction from MnO_2 to MnO, indicating that a substantial fraction of Mn^{3+} accompanied with oxygen vacancies exists in all these $y$$CuO_x$/OMS-2 samples. Among them, 0.05CuO_x/OMS-2 gave the lowest amounts of H_2 consumption (8.8 mmol·g^{-1}). These above-mentioned results showed that doping of Cu species enhances the reducibility and reactivity of the catalysts.

The O_2-TPD tests were conducted over the unsupported OMS-2 material and yCuO_x/OMS-2 catalysts to probe their differences in the release of oxygen. There are several peaks that can be found in the O_2-TPD curves of all samples and fitted as shown in Figure 5b, which were assigned to the release of surface-adsorbed oxygen species (O_{ads}) at 100 °C, surface lattice oxygen species (surf. O_{lat}) at 300−400 °C, subsurface (sub-surf. O_{lat}) and bulk lattice oxygen (bulk O_{lat}) in the transformation process of MnO_2 to MnO above 400 °C.[34,53−55] Nevertheless, a small peak at ca. 550 °C appeared in all these $y$$CuO_x$/OMS-2 samples, which was absent in the case of unsupported OMS-2, suggesting that this peak could be ascribed to the Cu species-bonding lattice oxygen (Cu-O_{lat}). Unfortunately, no obvious shift of these peaks could be observed with the addition of Cu species in $y$$CuO_x$/OMS-2 compared to the unsupported OMS-2. However, differences in their peak areas could be discovered based on these fitted results. It is worth noting that excluding the case of 0.1CuO_x/OMS-2, the content of surface lattice oxygen species gradually increased as the Cu/Mn ratios increased from 0.01 to 0.05, indicating that the lability of oxygen has been improved and more oxygen vacancies could be formed. As shown in Figure 5b, the 0.05CuO_x/OMS-2 catalyst gave the highest content of surface oxygen species, which could be accounted for the optimum performance in the ozone catalytic decomposition. However, the content of surface oxygen species in 0.1CuO_x/OMS-2 was obviously smaller than its counterparts and even the unsupported OMS-2 material, probably due to the much smaller specific surface area in the former compared to that of the latter, which is unfavorable to expose the active surface oxygen. These results also proved that the strong Cu−Mn interaction increased and doping Cu species accelerated the formation of surface lattice oxygen vacancies.

https://doi.org/10.1021/acsomega.3c01186
ACS Omega 2023, 8, 19632−19644

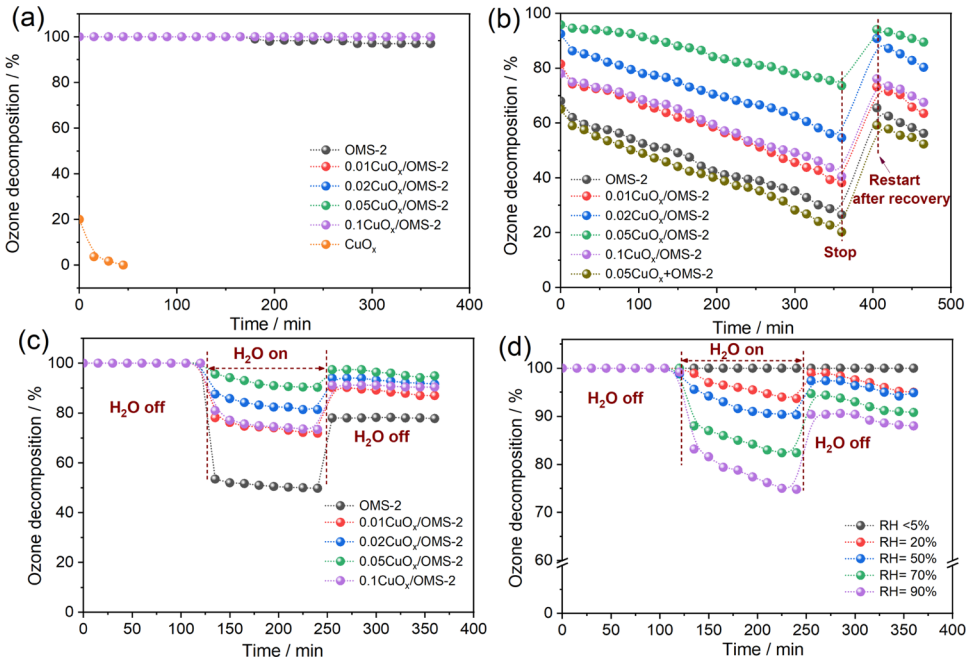

Figure 7. Performance of various samples for ozone removal in a dry atmosphere (RH < 5%) (a); humid conditions (RH = 50%) (b); alternatively in humid (RH = 50%) and dry (RH < 5%) atmospheres (c); and 0.05CuO_x/OMS-2 catalyst in different humidity atmospheres (d). Conditions: ozone concentration: 50 ± 2 ppm, temperature: 25 °C, weight space velocity = 600 000 mL g^{-1} h^{-1}, and catalyst weight = 100 mg.

3.3. Surface Electronic State Analysis. The surface electronic states of the OMS-2 and $y$$CuO_x$/OMS-2 catalysts were also characterized by the XPS measurement as shown in Figure 6, and each component ratio is also listed in Table 2. As shown in Figure 6a, the Mn $2p_{3/2}$ spectrum was deconvoluted into two peaks with binding energies of 642.3 and 643.4 eV, which corresponded to Mn^{3+} and Mn^{4+}, respectively.[6,56] As listed in Table 2, the ratios of Mn^{3+} in all $y$$CuO_x$/OMS-2 catalysts (47.3−58.8%) were obviously higher than that of OMS-2 (39.8%), indicating that the addition of Cu species promotes the formation of Mn^{3+} in these catalysts. Among these, the 0.05CuO_x/OMS-2 catalyst contained the highest amount of Mn^{3+} (58.8%), which was consistent with the H_2-TPR and O_2-TPD results. A lot of previous studies suggested that the more the Mn^{3+} (surface oxygen vacancies) on the surface of the catalyst, the higher the activity for ozone decomposition.[22,27,57] This well explains the higher activity of 0.05CuO_x/OMS-2 in catalytic ozone decomposition than that of its counterparts. The average oxidation state (AOS) of Mn can also be determined by the energy difference (ΔEs) between the spin splitting peak of Mn 3s from Figure 6b, which can be calculated by using the following formula: AOS = 8.956 − 1.126 ΔEs.[22,27] As shown in Table 2, the calculated AOSs of surface Mn species in $y$$CuO_x$/OMS-2 catalysts were obviously lower than that of unsupported OMS-2. Among these, the AOSs of surface Mn species in 0.05CuO_x/OMS-2 were the lowest, ascribed to the presence of abundant Mn^{3+} (surface oxygen vacancy) as mentioned above.

For Cu 2p spectra, as shown in Figure 6c, the peaks at 933.6 and 953.6 eV were attributed to Cu $2p_{3/2}$ and $2p_{1/2}$, respectively.[30] In addition, two typical strong Cu^{2+} satellite peaks[58] also appear at binding energies of 943.8 and 962.8 eV, indicating that a plenty of Cu^{2+} species exist in these CuO_x nanosheets. However, the possibility of other Cu species such as Cu^{+} cannot be ruled out. Therefore, the Auger Cu LMM spectrum was also employed to determine the different ratios of Cu^{2+} and Cu^{+} species on these samples surface, as shown in Figure 6d. The Cu LMM spectrum can be deconvoluted into two peaks at a kinetic energy of 916.7 and 917.6 eV, assigning to Cu^{+} and Cu^{2+} species, respectively.[59] Their ratios were also calculated based on the results of the Cu LMM spectrum. As shown in Table 2, excluding the case of 0.1CuO_x/OMS-2, the Cu^{2+} ratio in the samples increases with the decrease of Mn^{4+}, signifying that there is growing strong interaction between Cu and Mn species, which enhances the redox ability of the catalyst, thus facilitating the ozone catalytic decomposition.

There are mainly two oxygen species in the O 1s spectrum as shown in Figure 6e. The peak appearing at 529.6 eV was ascribed to lattice oxygen (O_α), while the peak of 531.3 eV was ascribed to the surface oxygen (O^-, O^{2-}) adsorbed on the oxygen vacancy (O_β).[25,60] Among these, the surface oxygen was considered to have a great influence on the ozone catalytic decomposition, as the high amount of surface oxygen is beneficial for the desorption of the intermediate product of oxygen species, thus promoting the decomposition rate of ozone.[27−29] As shown in Table 2, it can be seen that excluding the case of 0.1CuO_x/OMS-2, the concentration of surface oxygen species in the CuO_x/OMS-2 catalysts increased significantly compared to those of the OMS-2 sample, indicating that the addition of Cu species was conducive to generating rich oxygen vacancies, which was in good agreement with the O_2-TPD results. Among these catalysts, the 0.05CuO_x/OMS-2 catalyst gave the largest amount of surface oxygen, consistent with the previous results. In addition, it was previously reported that the remaining K species in these catalysts were unfavorable for the formation of surface oxygen vacancies. However, in this work, the effect of the remaining K species on the samples could be ruled out, as there was no obvious difference in K/Mn molar ratios between OMS-2 and $y$$CuO_x$/OMS-2 catalysts as listed in Table 2.

3.4. Catalytic Activity of Ozone Decomposition. Figure 7a shows the catalytic activity of ozone decomposition

https://doi.org/10.1021/acsomega.3c01186
ACS Omega 2023, 8, 19632−19644

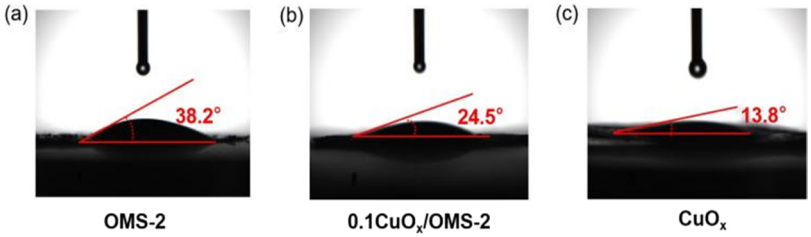

Figure 8. Water contact angle measurements of OMS-2 (a), 0.1CuO_x/OMS-2 (b), and CuO_x powders (c).

over various samples under a dry atmosphere (RH < 5%). The ozone conversion of the OMS-2 sample was maintained over 95% in 6 h, whereas the pure CuO_x was by far the least active even under a dry atmosphere, as shown in Figure 7a. However, all of the $y$$CuO_x$/OMS-2 catalysts converted ozone to ∼100% in 6 h when operating under a dry atmosphere.

The catalytic behaviors of ozone decomposition over various samples under dry humid conditions (RH = 50%) are also illustrated in Figure 7b. In contrast to the dry atmosphere depicted in Figure 7a, the obvious deactivation of all these catalysts under humid conditions could be observed probably due to the gradually covered oxygen vacancy by H_2O. Among these, the 0.05CuO_x/OMS-2 catalyst outperformed the others in terms of ozone decomposition activity and stability, indicating its best activity and resistance to water. It is also interesting to note that the CuO_x and OMS-2 physical mixing sample (labeled as 0.05CuO_x + OMS-2) gave lower ozone conversion and worse water resistance than those of pure OMS-2 and all other $y$$CuO_x$/OMS-2 catalysts, indicating that only the strong interaction formed between Cu and Mn species is favorable for improvement of the catalytic performance. In order to clearly understand the deactivation of the catalyst, these spent catalysts (under RH = 50%, for 6 h) were regenerated by heating at 110 °C overnight. Furthermore, it could be found that the conversion of ozone could be recovered to 95% just as the fresh catalyst in the initial step, and thus, it seems to be speculated that the main reason for the obvious deactivation of the fresh catalyst under humid conditions could be the adsorption of water vapor on the surface of these catalysts.

Figure 7c shows the the ozone conversions of various samples alternatively in a dry (RH < 5%) atmosphere and humid (RH = 50%) one. As shown in Figure 7c, the catalytic activity of the OMS-2 sample decreased sharply to about 50%, once switching the dry gas conditions (RH < 5%) to humid gas conditions (RH = 50%), while that of $y$$CuO_x$/OMS-2 is still above 70%, indicating that the Cu species promote the OMS-2 for ozone catalytic decomposition with improved water resistance. Among these, the 0.05CuO_x/OMS-2 catalysts showed the best activity for ozone decomposition with an ozone conversion above 90%, which may be ascribed to the highest content of surface oxygen vacancies. The results indicate that doping with Cu species in OMS-2 could promote the water resistance. Nevertheless, it was noted that once the RH was switched from humid gas (RH = 50%) to the dry gas conditions (RH < 5%), the ozone decomposition activity of the $y$$CuO_x$/OMS-2 catalyst was hardly restored to the original stage, which suggested that the accumulated adsorbed water molecules on the surface of these catalysts account for the obvious deactivation.

Since the water vapor has a severe influence on the catalytic performance in ozone decomposition, the study of the effect of relative humidity (RH) on the ozone catalytic performance of the 0.05CuO_x/OMS-2 catalyst was also characterized under different RH conditions, i.e., <5, 20, 50, 70, and 90%. As shown in Figure 7d, it is obvious that the ozone decomposition activity of 0.05CuO_x/OMS-2 strongly depends on the RH. The higher the humidity, the faster the deactivation. To make matters worse, their activity performance could not be restored to the initial stage once the atmosphere was switched from humid gas conditions to dry gas conditions, especially under the RH of 90%. Previous studies have confirmed that the water molecules adsorbed on the surface oxygen vacancy can lead to the loss of active sites by competitive adsorption with ozone.[57]

3.5. Ozone Catalytic Decomposition Mechanism. On the basis of the above-mentioned characterization results, it was strongly dictated that Cu species in these $y$$CuO_x$/OMS-2 catalysts mainly exist as two different states. One part of Cu species aggregated on the surface of OMS-2 to form dispersed CuO_x nanosheets, then attached, and were located at the external surface of OMS-2 as demonstrated by XRD (Figure 1a), FESEM results (Figure 2), and N_2 adsorption−desorption analysis (Figure 3). The other part of Cu species as ionic Cu entered the MnO_6 octahedral framework of OMS-2 near the catalyst surface to replace the Mn species, which promote the formation of Mn^{3+} and surface oxygen vacancy as demonstrated by Raman (Figure 1b), H_2-TPR (Figure 4a), O_2-TPD (Figure 4b), and XPS results (Figure 5). Based on the catalytic results, it is safe to conclude that the addition of Cu species in OMS-2 could obviously promote the ozone catalytic decomposition with improved water resistance compared to the unsupported OMS-2. Among these catalysts, 0.05CuO_x/OMS-2 shows superior activity, which could be mainly related to the relatively highest amount of surface oxygen vacancies, which enhance the activation of ozone decomposition and were considered as the active sites for ozone catalytic decomposition.[27,52]

It is worth noting that the 0.1CuO_x/OMS-2 catalyst still exhibited much higher catalytic performance with improved water resistance than that of unsupported OMS-2 materials, even though the ratio of the surface oxygen vacancy (O_β) over the former could not be effectively improved by the substitution for Mn^{4+} with Cu^{2+} compared to that of the latter as shown in Table 2. The reason could be related to the existence of excess Cu species such as CuO nanosheets located on the surface of the former while being absent over the latter, indicating that there could be other key factors which also exerted an effect on the catalytic performance under humidity conditions, such as the surface hydrophilicity depending on different materials. It was reported that H_2O molecules could be apt to suppress the surface oxygen vacancy, thus blocking the exposed active sites of OMS-2-based materials.[21] Therefore, the difference of surface hydrophilicity between OMS-2 and CuO_x nanosheets located on the catalyst surface may result

https://doi.org/10.1021/acsomega.3c01186
ACS Omega 2023, 8, 19632−19644

in the different affinities of H_2O molecules. For this, both the water contact angle and H_2O-TPD measurements of unsupported OMS-2 materials, $0.1CuO_x$/OMS-2 catalysts, and CuO_x powders were characterized to confirm the differences of surface hydrophilicity in a more intuitive way. As shown in Figure 8, the water contact angles on OMS-2, $0.1CuO_x$/OMS-2, and CuO_x were 38.2, 24.8, and 13.8° respectively, indicating that the CuO_x was much more sensitive to H_2O, which could be accounted for the smaller water contact angles on the $0.1CuO_x$/OMS-2 compared to that of unsupported OMS-2. Meanwhile, H_2O-TPD over these samples is also illustrated in Figure 9. These desorption

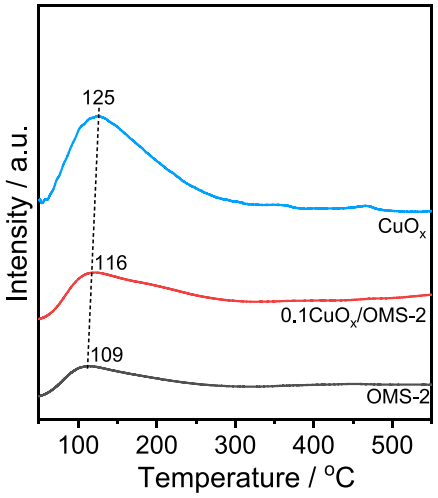

Figure 9. H_2O-TPD of OMS-2, $0.1CuO_x$/OMS-2, and CuO_x powders.

peaks were observed to shift from 109 to 116 to 125 °C over OMS-2, $0.1CuO_x$/OMS-2, and CuO_x, respectively, and gradually broadened. These results indicated that both the strength and amount of H_2O adsorption increase as the amount of CuO_x increased. In other words, H_2O was more easily and strongly adsorbed on CuO_x compared to the unsupported OMS-2; thus, CuO_x nanosheets located at the external surface of OMS-2 are more inclined to adsorb the H_2O from the atmosphere. Thus, it is possible for the CuO nanosheets to serve as non-oxygen vacancy sites for H_2O adsorption over these $yCuO_x$/OMS-2 catalysts, which could alleviate the catalyst deactivation to some extent caused by occupancy of H_2O on surface oxygen vacancies, thus efficiently preventing water from accumulating on the exposed surface oxygen vacancies against water poisoning. For the unsupported OMS-2 materials, the H_2O from the atmosphere can only occupy the surface oxygen vacancy of OMS-2, thus resulting in lower activity and poor water resistance.

Herein, considering the revealed above-mentioned results, we believed that the surface oxygen vacancies acted as active sites for ozone catalytic decomposition irrespective of it being over unsupported OMS-2 or $yCuO_x$/OMS-2 catalysts. Taking the CuO_x/OMS-2 catalysts for example, the possible reaction mechanism of ozone decomposition over these samples could be depicted as three steps (expressed as eqs 2−4) under a dry atmosphere, similarly as proposed by others.[26,27] First, once the samples are brought into contact with ozone, the ozone molecule (O_3) inserts one oxygen atom into the surface oxygen vacancy, thus forming a surface-bound oxygen species (O^{2-}) at the oxygen vacancy site and releasing a dioxygen molecule (O_2), which desorbs into the gas phase (see eq 2). Second, another ozone molecule reacts with the surface-bound oxygen species (O^{2-}) to produce a peroxide (O_2^{2-}) species and a dioxygen molecule (O_2) (see eq 3). Finally, the peroxide (O_2^{2-}) species decomposes and desorbs a dioxygen molecule (O_2), and consequently, the oxygen vacancy is recovered (see eq 4), which completes the cycle of catalytic decomposition of ozone and then in turn participates in the next cycle.

$$Cu^{1+} - V_O - Mn^{3+} + O_3 \rightarrow Cu^{2+} - O^{2-} - Mn^{4+} + O_2 \quad (2)$$

$$Cu^{2+} - O^{2-} - Mn^{4+} + O_3 \rightarrow Cu^{2+} - O_2^{2-} - Mn^{4+} + O_2 \quad (3)$$

$$Cu^{2+} - O_2^{2-} - Mn^{4+} \rightarrow Cu^{1+} - V_O - Mn^{3+} + O_2 \quad (4)$$

Among these, V_O represents the surface oxygen vacancy formed by the substitution for Mn^{4+} with Cu^{2+} as ionic Cu species entering the MnO_6 octahedral framework of OMS-2 to maintain charge balance. Nevertheless, in the presence of H_2O, the reaction pathways for ozone catalytic decomposition over unsupported OMS-2 and $yCuO_x$/OMS-2 could be modified as demonstrated in Scheme 2. As shown in Scheme 2a, the competitive adsorption of H_2O and O_3 over unsupported OMS-2 leads to some oxygen vacancies being occupied by H_2O, resulting in the decrease of active sites bound to O_3, thus reducing the decomposition activity of ozone. However, the enhancement of the catalytic ozone decomposition performance of $yCuO_x$/OMS-2 may be ascribed to two aspects as shown in Scheme 2b. On the one hand, the addition of Cu species obviously promotes the formation of the surface oxygen vacancies (Cu^{1+}−V_O−Mn^{3+}) due to the more surface oxygen vacancies as active centers produced, which are favorable to enhance the catalytic activity of ozone decomposition. On the other hand, the CuO nanosheets

Scheme 2. Schematic Representation of the Possible Ozone Catalytic Decomposition Mechanism over Unsupported OMS-2 (a) and CuO_x/OMS-2 Catalysts (b) under Humid Conditions

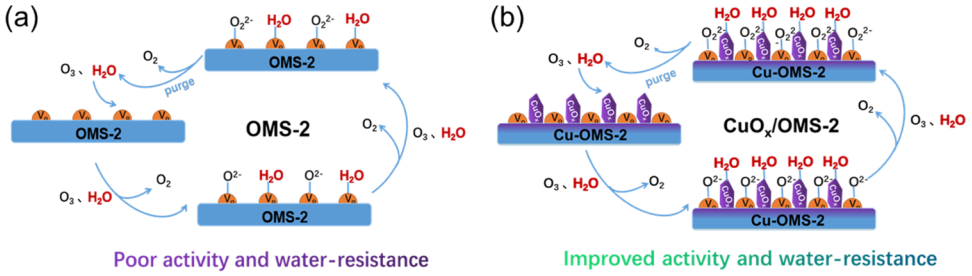

https://doi.org/10.1021/acsomega.3c01186
ACS Omega 2023, 8, 19632−19644

served as non-oxygen vacancy sites for H_2O adsorption over the catalyst to alleviate the catalyst deactivation aroused from some surface oxygen vacancies occupied by the H_2O from the atmosphere. Thanks to the combined effect of different Cu species, the OMS-2 materials modified with Cu species could obviously improve both the ozone decomposition activity and water resistance. Nevertheless, due to the hydrophilicity of the yCuO$_x$/OMS-2 catalyst, low stability for ozone decomposition under high humidity (RH = 90%) over these yCuO$_x$/OMS-2 could be observed. Therefore, the active OMS-2-based catalysts with high water resistance in high-moisture conditions (RH = 90%) still need further research.

4. CONCLUSIONS

In summary, we demonstrated that the OMS-2 materials modified with different contents of Cu species via an impregnation method could effectively improve both the decomposition activity of 50 ppm ozone and water resistance over the catalysts at a high weight hourly space velocity (WHSV) of 600 000 mL g^{-1} h^{-1} under the mild relative humidity (RH = 50%) and room temperature (25 °C). These CuO$_x$/OMS-2 catalysts exhibited dispersed CuO$_x$ nanosheets attached and located at the external surface of OMS-2 accompanied with ionic Cu species location within the framework of OMS-2. It was found that the promotion of ozone catalytic decomposition activity could be ascribed to the combined effect of these two different Cu species in these catalysts. Among these, ionic Cu replaces the Mn ions in the framework near the catalyst surface, thus resulting in an enhanced mobility of surface oxygen species and the formation of more oxygen vacancies, while the CuO$_x$ nanosheets located on the surface could serve as non-oxygen vacancy sites for H_2O adsorption due to their better hydrophilicity than that of OMS-2. Among these catalysts, the 0.05CuO$_x$/OMS-2 catalysts showed the best activity for ozone decomposition, due to its largest concentration of surface oxygen vacancies. Furthermore, we proposed two different reaction pathways for ozone catalytic decomposition over unsupported OMS-2 and CuO$_x$/OMS-2 in a humid atmosphere with the involvement of oxygen vacancies as well as the surface CuO$_x$ nanosheets. This work could provide a reference to the development of highly efficient catalysts for ozone decomposition under humid conditions.

AUTHOR INFORMATION

Corresponding Authors

Xiao Chen − *Jinhua Polytechnic, Jinhua 321007, People's Republic of China*; Email: morningchenxiao@163.com

Aiping Jia − *Key Laboratory of the Ministry of Education for Advanced Catalysis Materials, Zhejiang Key Laboratory for Reactive Chemistry on Solid Surfaces, Institute of Physical Chemistry, Zhejiang Normal University, Jinhua 321004, People's Republic of China*; orcid.org/0000-0002-9394-5585; Email: aipingjia@zjnu.cn

Authors

Chonglai Chen − *Jinhua Polytechnic, Jinhua 321007, People's Republic of China*

Jun Xie − *Wenzhou Water Supply Co. Ltd., Wenzhou 325000, People's Republic of China*

Wenxia Zhang − *Jinhua Polytechnic, Jinhua 321007, People's Republic of China*

Jian Chen − *Key Laboratory of the Ministry of Education for Advanced Catalysis Materials, Zhejiang Key Laboratory for Reactive Chemistry on Solid Surfaces, Institute of Physical Chemistry, Zhejiang Normal University, Jinhua 321004, People's Republic of China*; orcid.org/0000-0001-5982-044X

Complete contact information is available at: https://pubs.acs.org/10.1021/acsomega.3c01186

Notes

The authors declare no competing financial interest.

ACKNOWLEDGMENTS

This work was supported by the Key and General Project of Jinhua Science and Technology Bureau (Nos. 2021C22562, 2021-4-334, 2021-4-335, 2022-4-006) and the National Natural Science Foundation of China (No. 21902146).

REFERENCES

(1) Yue, X.; Unger, N.; Harper, K.; Xia, X. G.; Liao, H.; Zhu, T.; Xiao, J. F.; Feng, Z. Z.; Li, J. Ozone and Haze Pollution Weakens Net Primary Productivity in China. *Atmos. Chem. Phys.* **2017**, *17*, 6073−6089.

(2) Fuhrer, J. Ozone Risk for Crops and Pastures in Present and Future Climates. *Naturwissenschaften* **2009**, *96*, 173−194.

(3) Niu, Y.; Chen, R. J.; Xia, Y. J.; Cai, J.; Lin, Z. J.; Liu, C.; Chen, C.; Peng, L.; Zhao, Z. H.; Zhou, W. H.; Chen, J. M.; Kan, H. D. Personal Ozone Exposure and Respiratory Inflammatory Response: The Role of DNA Methylation in the Arginase−Nitric Oxide Synthase Pathway. *Environ. Sci. Technol.* **2018**, *52*, 8785−8791.

(4) Li, H. Y.; Wu, S. W.; Pan, L.; Xu, J. H.; Shan, J.; Yang, X.; Dong, W.; Deng, F. R.; Chen, Y. H.; Shima, M.; Guo, X. Short-term Effects of Various Ozone Metrics on Cardiopulmonary Function in Chronic Obstructive Pulmonary Disease Patients: Results from a Panel Study in Beijing, China. *Environ. Pollut.* **2018**, *232*, 358−366.

(5) Gong, S. Y.; Li, W. H.; Xie, Z.; Ma, X.; Liu, H. D.; Han, N.; Chen, Y. F. Low temperature Decomposition of Ozone by Facilely Synthesized Cuprous Oxide Catalyst. *New J. Chem.* **2017**, *41*, 4828−4834.

(6) Yang, L.; Ma, J.; Li, X.; He, G.; Zhang, C.; He, H. Improving the Catalytic Performance of Ozone Decomposition over Pd-Ce-OMS-2 Catalysts under Harsh Conditions. *Catal. Sci. Technol.* **2020**, *10*, 7671−7680.

(7) Li, X.; Ma, J.; He, H. Recent Advances in Catalytic Decomposition of Ozone. *J. Environ. Sci.* **2020**, *94*, 14−31.

(8) Gong, S.; Chen, J.; Wu, X.; Han, N.; Chen, Y. In-situ Synthesis of Cu_2O/Reduced Graphene Oxide Composite as Effective Catalyst for Ozone Decomposition. *Catal. Commun.* **2018**, *106*, 25−29.

(9) Mathew, T.; Suzuki, K.; Ikuta, Y.; Nagai, Y.; Takahashi, N.; Shinjoh, H. Mesoporous Ferrihydrite-Based Iron Oxide Nanoparticles as Highly Promising Materials for Ozone Removal. *Angew. Chem., Int. Ed.* **2011**, *50*, 7381−7384.

(10) Gong, S. Y.; Wang, A.; Wang, Y.; Liu, H.; Han, N.; Chen, Y. Heterostructured Ni/NiO Nanocatalysts for Ozone Decomposition. *ACS Appl. Nano Mater.* **2020**, *3*, 597−607.

(11) Yu, Y.; Liu, S.; Ji, J.; Huang, H. Amorphous MnO_2 Surviving Calcination: an Efficient Catalyst for Ozone Decomposition. *Catal. Sci. Technol.* **2019**, *9*, 5090−5099.

(12) Ji, J.; Fang, Y.; He, L. S.; Huang, H. B. Efficient Catalytic Removal of Airborne Ozone under Ambient Conditions over Manganese Oxides Immobilized on Carbon Nanotubes. *Catal. Sci. Technol.* **2019**, *9*, 4036−4046.

(13) Yu, Q.; Pan, H.; Zhao, M.; Liu, Z.; Wang, J.; Chen, Y.; Gong, M. Influence of Calcination Temperature on the Performance of Pd−Mn/SiO_2−Al_2O_3 Catalysts for Ozone Decomposition. *J. Hazard. Mater.* **2009**, *172*, 631−634.

https://doi.org/10.1021/acsomega.3c01186
ACS Omega 2023, 8, 19632−19644

(14) Hao, Z.; Cheng, D.; Guo, Y.; Liang, Y. Supported Gold Catalysts Used for Ozone Decomposition and Simultaneous Elimination of Ozone and Carbon Monoxide at Ambient Temperature. *Appl. Catal., B* **2001**, *33*, 217−222.
(15) Batakliev, T.; Tyuliev, G.; Georgiev, V.; Anachkov, M.; Eliyas, A.; Rakovsky, S. Ozone Decomposition Reaction over α-Alumina-Supported Silver Catalyst: Comparative Study of Catalytic Surface Reactivity. *Ozone Sci. Eng.* **2015**, *37*, 216−220.
(16) Lian, Z.; Ma, J.; He, H. Decomposition of High-Level Ozone Under High Humidity over Mn−Fe Catalyst: The Influence of Iron Precursors. *Catal. Commun.* **2015**, *59*, 156−160.
(17) Tang, W. X.; Liu, H. D.; Wu, X. F.; Chen, Y. F. Higher Oxidation State Responsible for Ozone Decomposition at Room Temperature over Manganese and Cobalt Oxides: Effect of Calcination Temperature. *Ozone Sci. Eng.* **2014**, *36*, 502−512.
(18) Dong, C.; Yang, J.-J.; Xie, L.-H.; Cui, G.; Fang, W.-H.; Li, J.-R. Catalytic Ozone Decomposition and Adsorptive VOCs Removal in Bimetallic Metal-Organic Frameworks. *Nat. Commun.* **2022**, *13*, No. 4991.
(19) Mehandjiev, D.; Naydenov, A.; Ivanov, G. Ozone Decomposition, Benzene and CO Oxidation over $NiMnO_3$-Ilmenite and $NiMn_2O_4$-Spinel Catalysts. *Appl. Catal., A* **2001**, *206*, 13−18.
(20) Jiang, C.; Zhang, P.; Zhang, B.; Li, J.; Wang, M. Facile Synthesis of Activated Carbon-Supported Porous Manganese Oxide via in situ Reduction of Permanganate for Ozone Decomposition. *Ozone Sci. Eng.* **2013**, *35*, 308−315.
(21) Hong, W.; Ma, J.; Zhu, T.; He, H.; Wang, H.; Sun, Y.; Shen, F.; Li, X. To Enhance Water Resistance for Catalytic Ozone Decomposition by Fabricating H_2O Adsorption-Site in OMS-2 Tunnels. *Appl. Catal., B* **2021**, *297*, No. 120466.
(22) Peng, B.; Bao, W. J.; Wei, L. L.; Zhang, R. D.; Wang, Z. J.; Wang, Z. C.; Wei, Y. Highly Active OMS-2 for Catalytic Ozone Decomposition under Humid Conditions. *Pet. Sci.* **2019**, *16*, 912−919.
(23) Yang, L.; Ma, J. Z.; Li, X. T.; He, G. Z.; Zhang, C. B.; He, H. Tuning the Fill Percentage in the Hydrothermal Synthesis Process to Increase Catalyst Performance for Ozone Decomposition. *J. Environ. Sci.* **2020**, *87*, 60−70.
(24) Yang, L.; Ma, J. Z.; Li, X. T.; Zhang, C. B.; He, H. Enhancing Oxygen Vacancies of Ce-OMS-2 via Optimized Hydrothermal Conditions to Improve Catalytic Ozone Decomposition. *Ind. Eng. Chem. Res.* **2020**, *59*, 118−128.
(25) Ma, J.; Wang, C.; He, H. Transition Metal Doped Cryptomelane-type Manganese Oxide Catalysts for Ozone Decomposition. *Appl. Catal., B* **2017**, *201*, 503−510.
(26) Hong, W.; Zhu, T.; Sun, Y.; Wang, H.; Li, X.; Shen, F. Enhancing Oxygen Vacancies by Introducing Na^+ into OMS-2 Tunnels To Promote Catalytic Ozone Decomposition. *Environ. Sci. Technol.* **2019**, *53*, 13332−13343.
(27) Jia, J.; Zhang, P.; Chen, L. Catalytic Decomposition of Gaseous Ozone over Manganese Dioxides with Different Crystal Structures. *Appl. Catal., B* **2016**, *189*, 210−218.
(28) Jia, J.; Yang, W.; Zhang, P.; Zhang, J. Facile Synthesis of Fe-Modified Manganese Oxide with High Content of Oxygen Vacancies for Efficient Airborne Ozone Destruction. *Appl. Catal., A* **2017**, *546*, 79−86.
(29) Zhu, G.; Zhu, J.; Jiang, W.; Zhang, Z.; Wang, J.; Zhu, Y.; Zhang, Q. Surface Oxygen Vacancy Induced α-MnO_2 Nanofiber for Highly Efficient Ozone Elimination. *Appl. Catal., B* **2017**, *209*, 729−737.
(30) Yun, L.; Li, Y.; Zhou, C.; Lan, L.; Zeng, M.; Mao, M.; Liu, H.; Zhao, X. The formation of CuO/OMS-2 nanocomposite leads to a significant improvement in catalytic performance for NO reduction by CO. *Appl. Catal., A* **2017**, *530*, 1−11.
(31) Liu, X.-S.; Jin, Z.; Lu, J.; Wang, X.; Luo, M. Highly Active CuO/OMS-2 Catalysts for Low-Temperature CO Oxidation. *Chem. Eng. J.* **2010**, *162*, 151−157.
(32) Yu, S.-Q.; Liu, N.; Liu, M.-G.; Wang, L. Synthesis of Diaryl Sulfides Based on Copper-Doped OMS-2. *J. Chem. Res.* **2021**, *45*, 237−241.
(33) Han, J.; Shan, W.; Zhao, B.; Wang, Y.; Zhang, Q.; Qin, L.; Chen, W. Catalytic Performance and Sulfur Resistance of OMS-2 Modified by Copper for Mercury Removal at Low Temperature. *Fuel* **2023**, *332*, No. 126040.
(34) Wang, X.; Sun, Y.; Li, M.; Zhang, W.; Zhu, Y. Excellent Catalytic Oxidation Performance on Toluene and Benzene over OMS-2 with a Hierarchical Porous Structure Synthesized by a One-pot Facile Method: Modifying Surface Properties by Introducing Different Amounts of K. *Catal. Sci. Technol.* **2022**, *12*, 2872−2886.
(35) Baek, S.; Myoung, J. Enhanced Luminescence of Quasi-Double Heterostructured Violet Light-Emitting Diodes Based on n-$Mg_{0.027}Zn_{0.973}O$ QD and p-$Cu_{1-x}Zn_xI$ Thin Films Fabricated via Simple Thermal Diffusion and Iodination Processes. *Chem. Eng. J.* **2021**, *413*, No. 127401.
(36) Feng, Q.-r.; Guo, J.; Xu, X.; Zhang, N.; Zhu, X.; Feng, S. The effect of ionic radius of metal element (M) on (Pb,M)-1212 superconductors (M = Sr, Ca, Mg, Hg, Cd, Cu). *Solid State Commun.* **1995**, *94*, 21−25.
(37) Yang, J.; Zhou, H.; Wang, L.; Zhang, Y.; Chen, C.; Hu, H.; Li, G.; Zhang, Y.; Ma, Y.; Zhang, J. Co Doped K-OMS-2 Nanofiber: A Novel and Efficient Water-Tolerant Catalyst for CO Oxidation. *ChemCatChem* **2017**, *9*, 1163−1167.
(38) Wang, R.; Li, J. Effects of Precursor and Sulfation on OMS-2 Catalyst for Oxidation of Ethanol and Acetaldehyde at Low Temperatures. *Environ. Sci. Technol.* **2010**, *44*, 4282−4287.
(39) Malinger, K.; Ding, Y.; Sithambaram, S.; Espinal, L.; Gomez, S.; Suib, S. Microwave Frequency Effects on Synthesis of Cryptomelane-Type Manganese Oxide and Catalytic Activity of Cryptomelane Precursor. *J. Catal.* **2006**, *239*, 290−298.
(40) Polverejan, M.; Villegas, J. C.; Suib, S. L. Higher Valency Ion Substitution into the Manganese Oxide Framework. *J. Am. Chem. Soc.* **2004**, *126*, 7774−7775.
(41) Wang, R. H.; Li, J. H. OMS-2 Catalysts for Formaldehyde Oxidation: Effects of Ce and Pt on Structure and Performance of the Catalysts. *Catal. Lett.* **2009**, *131*, 500−505.
(42) Eren, B.; Heine, C.; Bluhm, H.; Somorjai, G. A.; Salmeron, M. Catalyst Chemical State during CO Oxidation Reaction on Cu(111) Studied with Ambient-Pressure X-ray Photoelectron Spectroscopy and Near Edge X-ray Adsorption Fine Structure Spectroscopy. *J. Am. Chem. Soc.* **2015**, *137*, 11186−11190.
(43) Hernández, W.; Centeno, M. A.; Sarria, F. R.; Ivanova, S.; Montes, M.; Odriozola, J. A. Modified Cryptomelane-type Manganese Dioxide Nanomaterials for Preferential Oxidation of CO in the Presence of Hydrogen. *Catal. Today* **2010**, *157*, 160−165.
(44) Liu, J.; Ke, L.; Sun, L.; Pan, F.; Yuan, X.; Xia, D. Unraveling the Multiple Roles of Ag Species Incorporation into OMS-2 for Efficient Catalytic Ozonation: Structural Properties and Mechanism Investigation. *J. Environ. Chem. Eng.* **2021**, *9*, No. 106199.
(45) Wang, L.; Wen, T.; Dong, H.; Zhan, J.; Long, C. Selective Catalytic Ozonation of Gaseous Ammonia to Dinitrogen on Cryptomelane-Type Manganese Oxide Catalysts: Role of Oxygen Vacancies and Acid Sites. *J. Cleaner Prod.* **2022**, *343*, No. 130906.
(46) Mazumdar, N. J.; Deshmukh, G.; Rovea, A.; Kumar, P.; Arredondo-Arechavala, M.; Manyar, H. Insights into Selective Hydrogenation of Levulinic Acid Using Copper on Manganese Oxide Octahedral Molecular Sieves. *R. Soc. Open Sci.* **2022**, *9*, No. 220078.
(47) King'ondu, C. K.; Opembe, N.; Chen, C.; Ngala, K.; Huang, H.; Iyer, A.; Garcés, H. F.; Suib, L. S. Manganese Oxide Octahedral Molecular Sieves (OMS-2) Multiple Framework Substitutions: A New Route to OMS-2 Particle Size and Morphology Control. *Adv. Funct. Mater.* **2011**, *21*, 312−323.
(48) Sahu, K.; Satpati, B.; Mohapatra, S. Facile Fabrication of CuO Nanosheets for Photocatalytic Applications. *Appl. Phys. A* **2021**, *127*, 361.
(49) Genuino, H. C.; Seraji, M. S.; Meng, Y. T.; Valencia, D.; Suib, S. L. Combined Experimental and Computational Study of CO Oxidation Promoted by Nb in Manganese Oxide Octahedral Molecular Sieves. *Appl. Catal., B* **2015**, *163*, 361−369.

https://doi.org/10.1021/acsomega.3c01186
ACS Omega 2023, 8, 19632−19644

(50) Meng, X.; Zhang, J.; Chen, B.; Jing, Z.; Zhao, P. Copper Supported on H^+-Modified Manganese Oxide Octahedral Molecular Sieves (Cu/H-OMS-2) as a Heterogeneous Biomimetic Catalyst for the Synthesis of Imidazo [1,2-a]-N-Heterocycles. *Catal. Sci. Technol.* **2016**, *6*, 890.
(51) Huang, Y.; Zheng, K.; Liu, X.; Meng, X.; Astruc, D. Optimization of Cu Catalysts for Nitrophenol Reduction, Click reaction and Alkyne Coupling. *Inorg. Chem. Front.* **2020**, *7*, 939−945.
(52) Yang, Y.; Huang, J.; Zhang, S.; Wang, S.; Deng, S.; Wang, B.; Yu, G. Catalytic Removal of Gaseous HCBz on Cu Doped OMS: Effect of Cu Location on Catalytic Performance. *Appl. Catal., B* **2014**, *150−151*, 167.
(53) Yang, W.; Su, Z.; Xu, Z.; Yang, W.; Peng, Y.; Li, J. H. Comparative Study of α-, β-, γ- and δ-MnO_2 on Toluene Oxidation: Oxygen Vacancies and Reaction Intermediates. *Appl. Catal., B* **2020**, *260*, No. 118150.
(54) Chen, B. B.; Wu, B.; Yu, L. M.; Crocker, M.; Shi, C. Investigation into the Catalytic Roles of Various Oxygen Species over Different Crystal Phases of MnO_2 for C_6H_6 and HCHO Oxidation. *ACS Catal.* **2020**, *10*, 6176−6187.
(55) Jia, J.; Zhang, P.; Chen, L. The Effect of Morphology of α-MnO_2 on Catalytic Decomposition of Gaseous Ozone. *Catal. Sci. Technol.* **2016**, *6*, 5841−5847.
(56) Liu, S.; Ji, J.; Yu, Y.; Huang, H. Facile Synthesis of Amorphous Mesoporous Manganese Oxides for Efficient Catalytic Decomposition of Ozone. *Catal. Sci. Technol.* **2018**, *8*, 4264−4273.
(57) Wei, Y.; Min, X.; Li, Y.; Wang, H.; Qi, F.; Liang, P.; Li, H.; Hu, J.; Sun, T. Modification of Manganese Oxides for Enhancing Ozone Catalytic Decomposition Under Moist Conditions. *Appl. Catal., A* **2022**, *640*, No. 118659.
(58) Li, X.; Kong, W.; Qin, X.; Qu, F.; Lu, L. Self-powered Cathodic Photoelectrochemical Aptasensor Based on *in* Situ−Synthesized CuO-Cu_2O Nanowire Array for Detecting Prostate-Specific Antigen. *Microchim. Acta* **2020**, *187*, 325.
(59) Peter, R.; Petravic, M. Initial Stages of Oxide Formation on Copper Surfaces during Oxygen Bombardment at Room Temperature. *J. Phys. Chem. C* **2021**, *125*, 25290−25297.
(60) Otto, K.; Haack, L. P.; Devries, J. E. Identification of Two Types of Oxidized Palladium on γ-alumina by X-ray Photoelectron Spectroscopy. *Appl. Catal., B* **1992**, *1*, 1−12.

https://doi.org/10.1021/acsomega.3c01186
ACS Omega 2023, 8, 19632−19644